

Distinguishing carrier transport and interfacial recombination at perovskite/transport-layer interfaces using ultrafast spectroscopy and numerical simulation

Edward Butler-Caddle¹,¹ K.D.G. Imalka Jayawardena^{1,2},² Anjana Wijesekara¹,¹ Rebecca L. Milot,¹ and James Lloyd-Hughes^{1,*}

¹Department of Physics, University of Warwick, Coventry, CV4 7AL, United Kingdom

²Advanced Technology Institute, University of Surrey, Guildford, GU2 7XH, United Kingdom

 (Received 5 February 2024; revised 31 May 2024; accepted 3 July 2024; published 6 August 2024)

In perovskite solar cells, photovoltaic action is created by charge transport layers (CTLs) either side of the light-absorbing metal halide perovskite semiconductor. Hence, the rates for desirable charge extraction and unwanted interfacial recombination at the perovskite-CTL interfaces play a critical role for device efficiency. Here, the electrical properties of perovskite-CTL bilayer heterostructures are obtained using ultrafast terahertz and optical studies of the charge carrier dynamics after pulsed photoexcitation, combined with a physical model of charge carrier transport that includes the prominent Coulombic forces that arise after selective charge extraction into a CTL, and cross-interfacial recombination. The charge extraction velocity at the interface and the ambipolar diffusion coefficient within the perovskite are determined from the experimental decay profiles for heterostructures with three of the highest-performing CTLs, namely C₆₀, PCBM and Spiro-OMeTAD. Definitive targets for the further improvement of devices are deduced: fullerenes deliver fast electron extraction, but suffer from a large rate constant for cross-interface recombination or hole extraction. Conversely, Spiro-OMeTAD exhibits slow hole extraction but does not increase the perovskite's surface recombination rate, likely contributing to its success in solar cell devices.

DOI: [10.1103/PhysRevApplied.22.024013](https://doi.org/10.1103/PhysRevApplied.22.024013)

I. INTRODUCTION

Perovskite solar cells first gained widespread attention when their power conversion efficiency jumped to over 10% by changing from a dye-sensitized structure incorporating a liquid, to an all solid-state design [1]. This structure remains the standard architecture to this day [2,3], and consists of a light-absorbing metal-halide perovskite sandwiched between an electron transporting layer (ETL) that selectively extracts conduction band electrons from the perovskite [but not valence band (VB) holes], and a hole transporting layer (HTL) that does the opposite, as pictured in Fig. 1. Employing interfaces of opposite selectivity on the two sides of the device gives photovoltaic action [4,5], which can be thought of as a kinetic asymmetry, and hence these heterojunctions are crucial to device performance. Selective extraction is enabled by a good

electronic band alignment for one band at the interface [e.g., perovskite conduction band and ETL lowest unoccupied molecular orbital (LUMO) in Fig. 1(a)], and the other band being misaligned [e.g., perovskite VB and ETL highest occupied molecular orbital (HOMO)]. Photovoltaic action also arises from the differences in the equilibrium Fermi levels of the different materials before they are connected [4,5] (particularly the electrodes), which creates a built-in field and an opposing gradient in chemical potential across the device when the layers are connected [6,7] [Fig. 1(b)]. Under illumination, the combined electrochemical potential develops a net gradient that drives electrons and holes towards different electrodes. Although photovoltaic action can occur without selective extraction layers, the charge carrier blocking function of the charge transport layers (CTLs) has been found to be crucial for high performance, by preventing electron-hole recombination processes at the electrodes that compete with power extraction [8–10]. As the quality of the perovskite layer has improved (i.e., recombination rate constants within the perovskite bulk have been reduced), the focus has shifted towards increasing the performance of CTLs [11–13]. A wide variety of CTL materials have been tested but those used in the earliest devices have remained among

*Contact author: j.lloyd-hughes@warwick.ac.uk

Published by the American Physical Society under the terms of the [Creative Commons Attribution 4.0 International](https://creativecommons.org/licenses/by/4.0/) license. Further distribution of this work must maintain attribution to the author(s) and the published article's title, journal citation, and DOI.

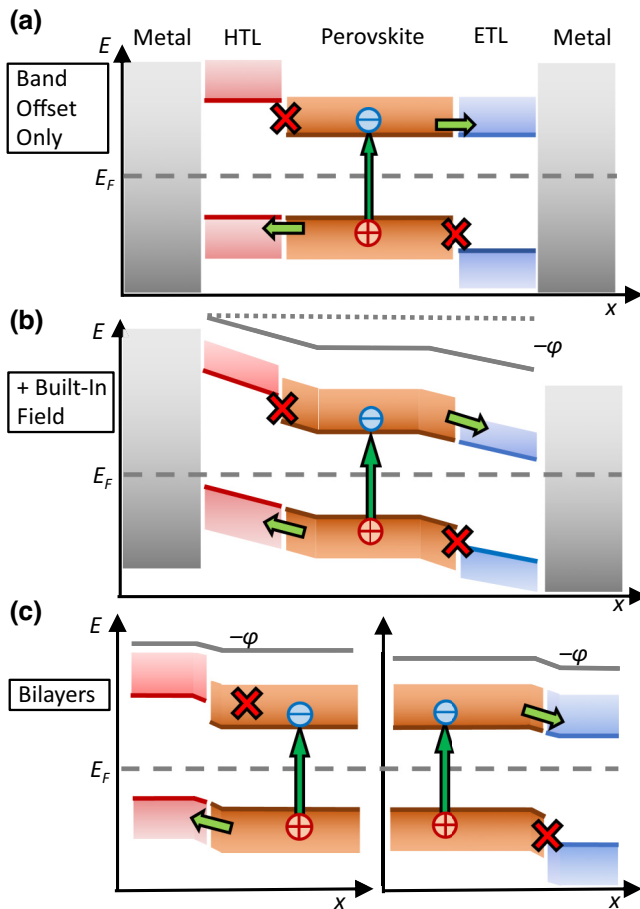


FIG. 1. (a),(b) Band diagrams for a typical perovskite solar cell geometry at equilibrium, with a hole transport layer (HTL) and electron transport layer (ETL) sandwiching the perovskite. (a) Kinetic asymmetry is induced by the band alignments of HTL and ETL relative to the perovskite. (b) The differences in Fermi level of each material create built-in electric fields, mostly due to the electrodes. (c) Band diagrams for a perovskite-HTL bilayer (left) and a perovskite-ETL bilayer (right), with small built-in fields confined to thin layers near the interfaces.

the most successful, namely the hole extracting material Spiro-OMeTAD, and the electron extracting materials C_{60} (fullerene molecule) and its derivative phenyl- C_{61} -butyric acid methyl ester (PCBM).

In order to make further increases in performance by design, rather than slow trial and error, the electrical properties of the heterojunctions formed by these CTLs should be understood, so that the limiting factors can be targeted for improvement. While measurements of the carrier dynamics of a complete device would be most representative of operational conditions, the large number of interfaces and processes present would make the dynamics difficult to interpret. Instead, by studying simple perovskite-CTL bilayers with one interface (for brevity shortened to CTL bilayers), the dynamics can be more easily interpreted and related to individual processes.

Although the built-in field in a bilayer will not be as large as in a full device [Figs. 1(b) and 1(c)], properties of individual interfaces derived from bilayer measurements can be readily transferred to a model of the full solar cell. Ideally, to uncover the diffusion coefficient and the kinetics of interfacial processes, studies of the carrier dynamics of bilayers should have excellent time resolution, well below 1 ns.

Here we report an investigation of the interfacial kinetics for perovskite-CTL bilayers fabricated from three of the highest-performing CTLs (C_{60} , PCBM and Spiro-OMeTAD) using time-resolved optical spectroscopy with photoluminescence, terahertz or visible white light probes. We elucidate the carrier dynamics on subnanosecond timescales using a physical model that, critically, includes the Coulombic forces between electrons and holes. This is vital for the description of interfacial kinetics when one charge carrier species is selectively extracted across an interface: for example, this can generate Coulomb forces that act as a bottleneck, switching off charge extraction. A quantitative agreement between the terahertz photoconductivity dynamics and the carrier dynamics model enabled the rate constants for surface extraction and cross-interface recombination to be determined, which revealed that C_{60} and PCBM both rapidly extract electrons, but unfortunately have sufficiently fast cross-interface recombination that no Coulomb bottleneck forms. In marked contrast, Spiro-OMeTAD did not rapidly extract holes from the perovskite, but did have a substantially slower surface extraction velocity and surface recombination velocity. The trends observed with subnanosecond terahertz and transient absorption measurements were also observed in nanosecond photoluminescence transients at lower injected carrier densities (comparable to solar illumination), indicating that the properties extracted from the subnanosecond measurements using higher injected carrier densities are relevant to operational carrier densities.

II. EXPERIMENTAL RESULTS

A. Heterojunction materials

For photovoltaics, the most directly relevant perovskite compositions to develop are those that have bandgaps close to the optimum calculated by the Shockley-Queisser model, while being sufficiently stable against degradation. One of the most promising routes to rapidly producing cells that exceed the efficiency of silicon cells is to form perovskite-silicon tandem cells, for which the Shockley-Queisser model gives an optimum perovskite bandgap of 1.6–1.7 eV [14,15], which requires mixed-halide compositions containing a majority of iodine and a minority of bromine. In this work, spin-coated thin films (for fabrication details see Appendix A) of triple cation mixed-halide perovskite were employed, with the composition

(FA_{0.83}MA_{0.17})_{0.95}Cs_{0.05}Pb(I_{0.83}Br_{0.17})₃. This composition has high crystallinity and excellent reproducibility and stability, including against light-induced halide segregation [16]. Electron micrographs [Figs. 2(a)–2(c)] showed complete coverage of the quartz substrates, with grain diameters of a few hundred nanometres, with most grains extending through the thickness of the layer (either 370 nm or 600 nm thick, depending on the batch).

After forming the perovskite thin films, different CTLs were deposited on top to form various perovskite-CTL bilayers. In the bilayers with spin-coated PCBM or Spiro-OMeTAD layers, the CTLs were approximately 120 nm thick, while thermally evaporated C₆₀ was 30 nm thick (atomic force microscope measurements confirmed complete coverage). These layers were thicker than used in solar cells, in order to ensure complete coverage of the underlying perovskite and thus avoid adding another variable (i.e., surface coverage) that can modify the dynamics (e.g., with incomplete coverage some carriers must travel

an additional distance to reach a perovskite-CTL heterojunction, and the carriers extracted into the CTL will be more concentrated). The ultrafast carrier dynamics should not be influenced by thicknesses above a few nanometres because within the 3 ns experimental time window, the low mobilities of the CTLs mean that extracted carriers will travel less than a few nanometres in fullerenes, and even less in Spiro-OMeTAD. To check whether the solution deposition of PCBM and Spiro-OMeTAD affected the underlying perovskite, perovskite layers washed with chlorobenzene were also prepared and measured, and showed no significant difference (see Supplemental Material [17], Figs. S8 and S9). Separately, reference CTLs were deposited directly on quartz to confirm their optical absorbance.

The UV and visible absorbance of the individual materials is reported in Fig. 2(d), showing that while PCBM and C₆₀ exhibit a small amount of absorption across the visible, Spiro-OMeTAD has strong absorption above 3.0 eV. The

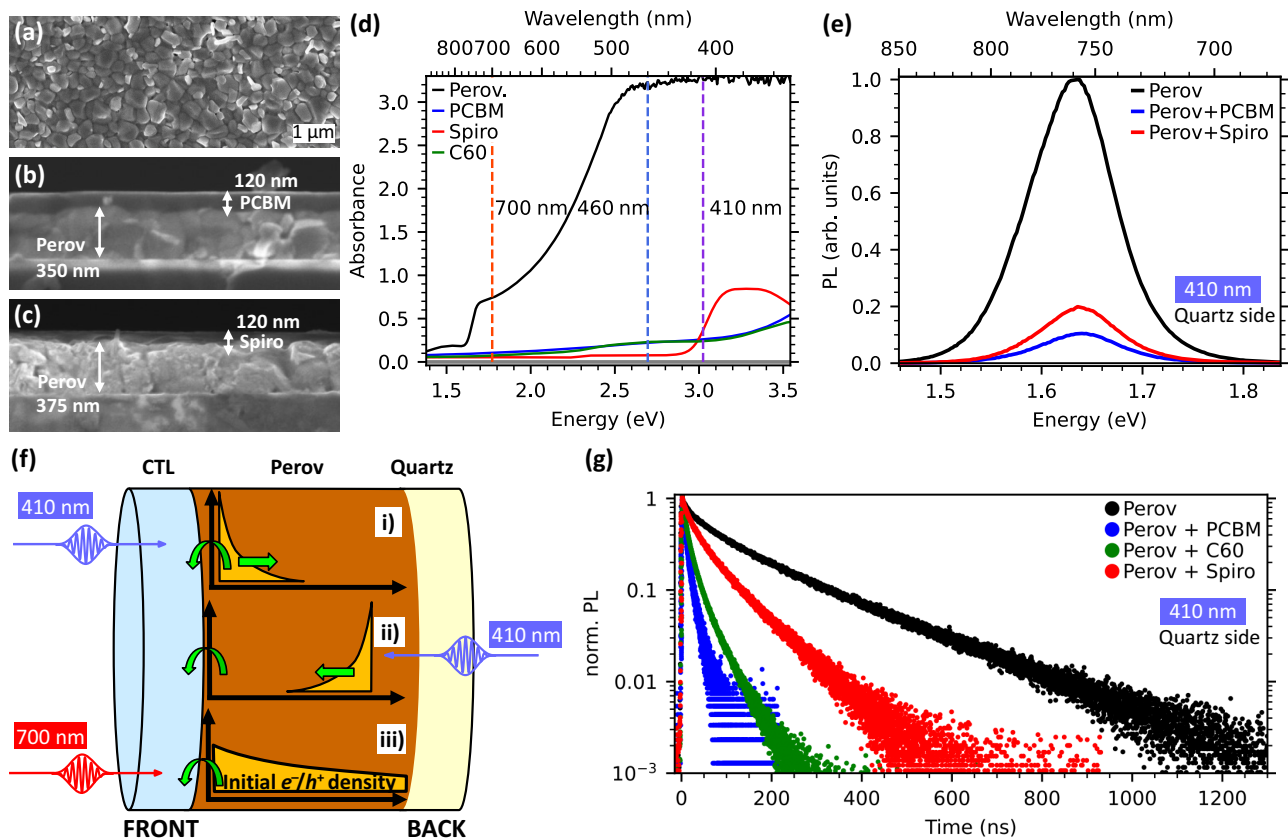


FIG. 2. (a)–(c) Representative scanning electron microscope (SEM) images of perovskite-CTL bilayers, showing: (a) grain morphology of the front surface; (b),(c) cross sections of perovskite-PCBM and perovskite-Spiro OMeTAD bilayers. (d) Absorbance spectra of individual materials used. The absorbance of the perovskite film (370 nm thick) at energies above 2.5 eV exceeded the maximum absorbance measurable with the spectrometer, and hence was estimated from that for thinner films (see Supplemental Material [17], Section 1.3). (e) Photoluminescence (PL) spectra of samples (600 nm thick) under 410-nm continuous-wave excitation from the back (quartz) side (approximately 400 W m⁻²). (f) Schematic of the different carrier profiles created with different pump wavelengths or excitation from alternate sides. (g) Time-resolved PL dynamics (at the peak PL energy) under 410 nm pulsed excitation from the back (370 nm thick).

triple-cation perovskite had a sharp absorption onset (band edge) near 1.6 eV and its steady-state photoluminescence (SS-PL) spectrum [Fig. 2(e)] peaked at 1.63 eV, which demonstrated this composition's suitable bandgap energy for tandem solar cells. Furthermore, SS-PL spectra showed no evidence of light-induced halide segregation as a second red-shifted peak did not appear under illumination, evidencing the long-term stability of this composition. The reduction in SS-PL intensities for the bilayers compared with the bare perovskite has been interpreted as an increase in nonradiative recombination channels when the CTLs are connected [18–20].

Throughout this paper, measurements on bare perovskite layers are plotted in black/gray, perovskite-PCBM bilayers are plotted in blue, perovskite-C₆₀ bilayers are plotted in green, and perovskite-Spiro-OMeTAD bilayers are plotted in red.

B. Time-resolved PL spectroscopy

In time-resolved optical spectroscopy a signal $S(t)$ related to the carrier density, n , in the perovskite layer is measured as a function of time t after photoexcitation, where S refers to either the PL intensity, transient absorption change, or terahertz photoconductivity [from optical pump terahertz probe (OPTP) spectroscopy], depending on the technique used. While in the reference perovskite material the carrier density can be altered only by bulk carrier recombination or surface recombination near the edges of the perovskite crystallites, in bilayers n can be additionally lowered by charge extraction into the CTL or by extra recombination at the CTL-perovskite interface. The experimental $S(t)$ corresponds to the total change integrated over the whole charge carrier distribution, and information about the density profile $n(x)$ with depth x is therefore lost from data at one time t . However, in certain situations the dynamical signal, $S(t)$, can still yield useful information about processes that occur at different depths in the bilayer, particularly if different photoexcitation schemes are used. As pictured in Fig. 2(f), illuminating with short wavelengths generates carriers in the perovskite near the CTL [case (i)], and hence the initial charge extraction and/or interfacial recombination rates should be high. At later times these rates should drop, as charges diffuse away from the heterojunction into the perovskite. In contrast, excitation through the substrate [case (ii)] yields carriers that are well separated from the CTL interface, with a low initial decay rate that then increases after carriers have had sufficient time to diffuse through the perovskite layer. Illuminating with long wavelengths [case (iii)] generates carriers throughout the depth of the perovskite layer, with similar dynamics expected to the long time limit for cases (i) and (ii).

Time-resolved PL dynamics measured by time-correlated single photon counting (TCSPC) are reported in Fig. 2(g) for the perovskite-CTL bilayers and bare

perovskite reference, recorded under 405-nm excitation from the quartz side with incident pulse fluences of 25 nJ cm⁻² (about 5×10^{14} incident photons per square meter per pulse) and under ambient conditions in order to passivate surface defects (see Appendix B). The injected carrier density is comparable to that under solar illumination, which for this triple-cation perovskite composition has been estimated as 4×10^{21} m⁻³ [21]. The modeling in Sec. III indicates that carriers spread throughout the layer thickness within the few-nanosecond resolution of TCSPC, so an approximately uniform density can be considered, which gives an injected density of 10^{21} m⁻³ for our TCSPC measurements.

The bare perovskite (black curve) had a PL lifetime of $\tau_{\text{eff}} = 200$ ns, consistent with results on a similar sample from electronically delayed OPTP (E-OPTP) with a long time window and low injection levels [22], which represents the effective lifetime from bulk recombination and any surface recombination at the perovskite-air or perovskite-substrate interfaces. When fullerene layers were added, the PL decay was significantly accelerated (blue and green curves), while the Spiro-OMeTAD bilayer (red) had only a marginally faster decay rate than the bare perovskite. The faster PL decay rates for the bilayers imply either charge extraction to the CTL or recombination at the CTL interface. The shortening of the PL decay time is consistent with the quenching of the SS-PL intensity.

For each sample no difference in PL dynamics was observed for photoexcitation on opposite sides, despite generating different initial distributions due to the short penetration depth ($\delta \sim 35$ nm) at this excitation wavelength. Furthermore, using excitation light with a longer penetration depth ($\delta \sim 260$ nm for 633-nm excitation) for each sample resulted in similar dynamics to that for 405-nm excitation (see Supplemental Material [17], Section 1.5). This implies that the instrument response time (several nanoseconds) was not sufficiently fast to distinguish case (i) (excitation on the front with short penetration depths), which should have much higher initial rates of extraction and interfacial recombination than cases (ii) and (iii) (excitation on back or excitation with long penetration depths). In short, the time taken for carriers to diffuse through the perovskite film is less than the instrument response time in these PL experiments, which therefore probed the later dynamics only.

C. Ultrafast spectroscopy

In order to investigate charge transport, charge extraction and interfacial recombination, we therefore turned to ultrafast pump-probe spectroscopies with subpicosecond time resolution. These were performed with incident pulse fluences of 2–7 $\mu\text{J cm}^{-2}$, corresponding to an incident photon flux of $0.6\text{--}1.4 \times 10^{17}$ m⁻² per pulse. The pump fluences for different wavelengths were chosen such

that the absorbed photon fluxes per pulse were similar for the different pump wavelengths (using the absorption data reported in Supplemental Material [17], Fig. S2 and S3). These low pump fluences were chosen such that the OPTP and transient absorption (TA) decay curves were flat for the bare perovskite sample (see Figs. 3 and 4), indicating that the fraction of the carrier population that recombines during the measurement window of 3 ns is negligible. This means recombination within the perovskite can be excluded, which significantly simplifies the interpretation

of the data. It is worth noting that the ultrafast dynamics were found to be more reproducible than time-resolved PL measurements performed at much lower pulse fluences of 25 nJ cm^{-2} (about 5×10^{14} incident photons per square meter per pulse).

1. Origin of the transient photoconductance

The OPTP decays reported in Fig. 3 show the change in transmitted electric field, $S(t) = -\Delta T/T$, which is

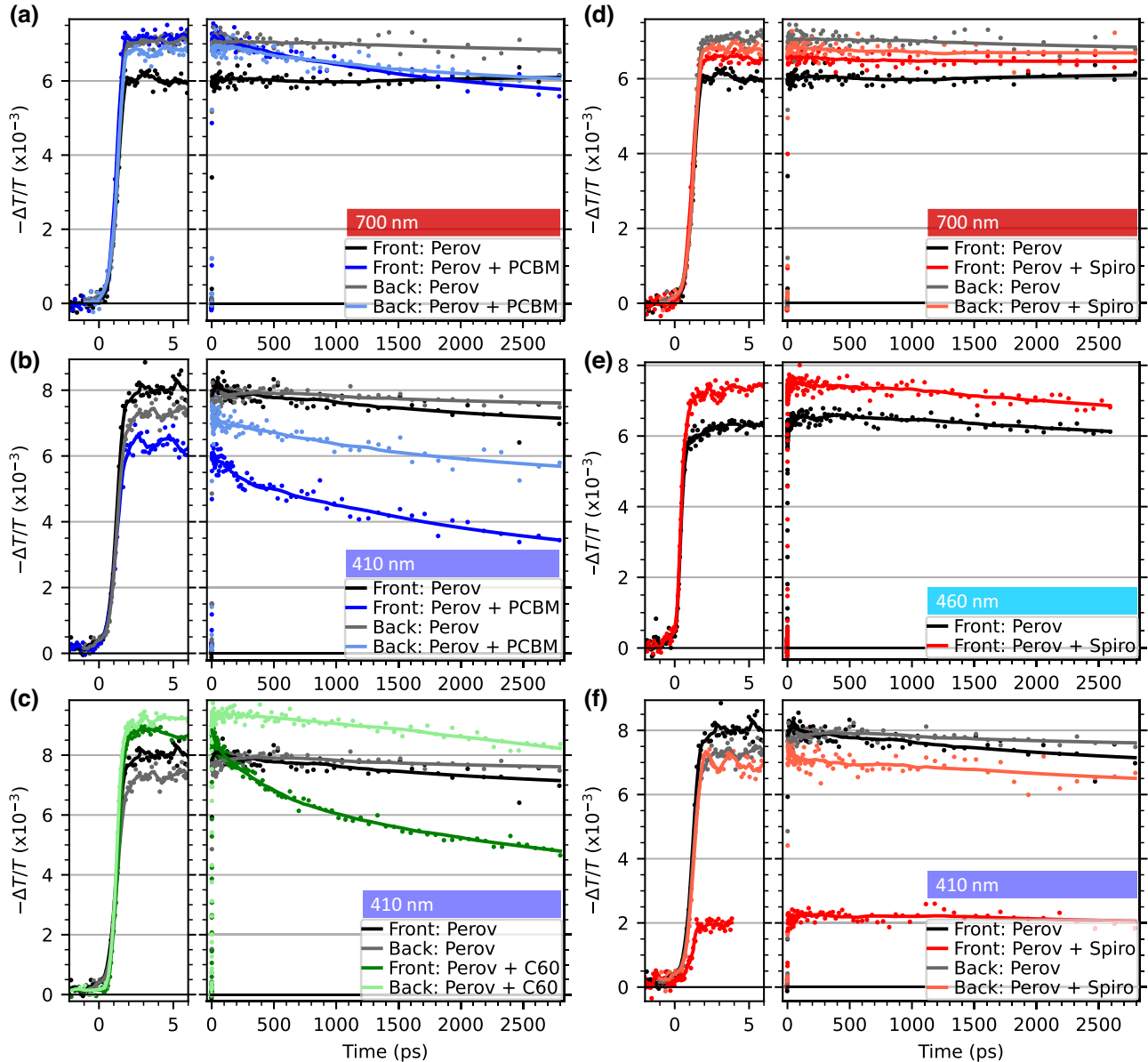


FIG. 3. (a)–(c) OPTP signal $S(t) = -\Delta T/T$ for perovskite-CTL bilayers with fullerene ETLs (C_{60} or PCBM) under different excitation wavelengths (all with incident pulse fluences of $2\text{--}7 \mu\text{J cm}^{-2}$, or $0.6\text{--}1.4 \times 10^{17}$ photons per square meter per pulse). Points show the raw data whereas the solid lines show a running average. Data for the bare perovskite reference (washed with chlorobenzene) are shown in black (front excitation) and gray (back excitation). Perovskite-PCBM bilayers are shown in blue, whereas C_{60} is shown in green, where darker and lighter shades indicate front and back excitation, respectively. (d)–(f) As (a)–(c), but for bilayers with the hole transporter Spiro-OMeTAD. All samples had 600-nm-thick perovskite, except that (e) was 370 nm thick.

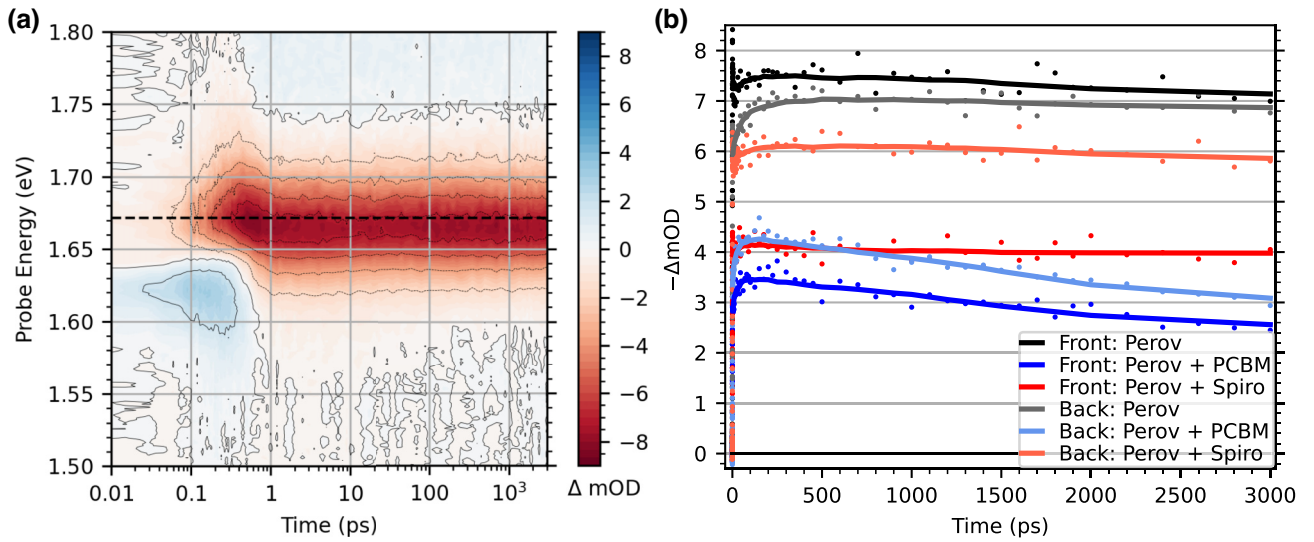


FIG. 4. (a) Transient absorption spectra ΔmOD versus probe energy and time delay for the perovskite reference (600 nm thick) with 410-nm excitation on the front (all with incident pulse fluences of $3 \mu\text{J cm}^{-2}$, or 7×10^{16} photons per square meter per pulse). The peak of the ground-state bleach (GSB) is illustrated by the dashed line. (b) Transient absorption dynamics at an energy of 1.67 eV (the GSB for the perovskite). Darker and lighter shades indicate front and back excitation respectively: black = perovskite reference (washed with chlorobenzene), blue = perovskite-PCBM bilayer, red = perovskite-Spiro-OMeTAD bilayer.

proportional to the sheet photoconductance $\Delta\sigma$ of the sample [22]. As the conductivity is $\sigma = ne\mu_e + pe\mu_h$, OPTP is sensitive to changes in either mobility or density, and hence we first establish the origin of $S(t)$ for CTL-perovskite bilayers. No appreciable contribution to the photoconductivity is expected from charges transferred to the CTLs, where carriers have a substantially lower mobility than in the perovskite: terahertz sum mobilities $\mu_e + \mu_h$ exceed $10 \text{ cm}^2 \text{ V s}^{-1}$ in perovskites [21], whereas Spiro-OMeTAD has $\mu_h < 10^{-3} \text{ cm}^2 \text{ V s}^{-1}$ [23] and PCBM exhibits $\mu_e < 1 \text{ cm}^2 \text{ V s}^{-1}$ [24–26].

To validate this assumption, in this work CTLs deposited on quartz were photoexcited above their bandgap (at 410 nm), and no CTL photoconductivity was observed via OPTP at the experimental fluences used. Hence, we conclude that $S(t)$ arises just from carriers in the perovskite film. Within the first picosecond following photoexcitation, the mobility of hot photoexcited carriers in the perovskite may change as carriers relax within the bandstructure [27,28] or into localized states [21]. However after this time the mobility can be assumed to be limited by electron-phonon scattering, and independent of time (and density), and thus changes in $-\Delta T/T$ are linked to the density of photoexcited carriers in the perovskite.

The sum of the electron and hole mobilities was calculated for the perovskite reference sample from the initial amplitude of the OPTP signal (method described in [29]), assuming unity quantum yield of free carriers (reasonable due to the low exciton binding energy in these perovskites [30]). This yielded a sum mobility of about $40 \text{ cm}^2 \text{ V}^{-1} \text{ s}^{-1}$ when using short pump wavelengths (and $70 \text{ cm}^2 \text{ V}^{-1} \text{ s}^{-1}$

when using long pump wavelengths), consistent with the literature [21]. Hence, the detected $S(t)$ from OPTP for bilayers can be safely assumed to arise only from the photoconductance of mobile charges in the perovskite films.

2. Transient photoconductance of perovskite-ETL bilayers

Figures 3(a)–3(c) report $S(t) = -\Delta T/T$ for the fullerene bilayers (C_{60} in green and PCBM in blue), which exhibited accelerated decay over the 3-ns window relative to the bare perovskite sample (black/gray), for both “front” excitation through the CTL (darker shade), and “back” excitation through the substrate (lighter shade).

For 700-nm excitation on the PCBM bilayer [case (iii), Fig. 3(a)], the initial amplitude and the decay dynamics for front excitation (dark blue) were similar to those for back excitation (light blue). This is consistent with the negligible parasitic absorption of this pump wavelength by the PCBM [Fig. 2(d)], and with the expectation that carrier removal dynamics will be similar when the electrons and holes are photoinjected throughout the layer (the perovskite’s absorption depth was about 260 nm). For excitation with 410 nm [Figs. 3(b) and 3(c)] on the front of the fullerene bilayers [case (i)], the decay was markedly faster than for 700-nm excitation: the carriers were concentrated near the interface rather than spread throughout the perovskite film’s thickness. The initial amplitude of the signal was marginally lower for excitation through the front [case (i), dark blue and green] than through the

back [case (ii), light blue and green], in agreement with parasitic absorption of the pump by the fullerenes [Fig. 2(d)].

For 410-nm excitation on the back [case (ii)] of the C₆₀ bilayer [light green, Fig. 3(c)], the decay rate was slow at early pump-probe delay times, before accelerating at later times. This can be qualitatively understood as requiring a finite time for carriers to diffuse from a low recombination velocity surface (perovskite-quartz interface) through the thickness of the film to the CTL interface, where population reduction can then occur. A quantitative model for both front and back excitation is discussed in Sec. III A. On the other hand, for 410-nm excitation on the back [case (ii)] of the PCBM bilayer [light blue, Fig. 3(b)], the dynamics was similar to that for 700-nm excitation. This suggests that the solution-deposited PCBM had penetrated deeper into the perovskite than the vapour-deposited C₆₀, thus reducing the distance carriers must diffuse from the quartz side to reach the PCBM.

3. Transient photoconductance of perovskite-HTL bilayer

The corresponding OPTP data for the Spiro-OMeTAD bilayer (hole extracting) are reported in Figs. 3(d)–3(f). In stark contrast to the case of electron extraction, there is no faster decay in the OPTP signal than in the perovskite reference over the 3-ns window, when excited on either side of the sample or with any of the pump wavelengths used (410 nm, 460 nm, and 700 nm). The only substantial difference is in the initial amplitude when exciting with 410 nm through the CTL: the Spiro-OMeTAD bilayer exhibited around 25% of the photoconductivity of the perovskite reference. In this case, a large fraction of the optical pump beam was absorbed by the Spiro-OMeTAD layer first, as Spiro-OMeTAD exhibits a substantial absorbance for that pump photon energy [Fig. 2(d); 410 nm corresponds to 3.02 eV]. For excitation conditions that did not exhibit parasitic absorption (700-nm and 460-nm excitation from either side and 410-nm back excitation) the similar initial amplitude to that of the bare perovskite, and the lack of decay within the 3-ns window, suggest that there is no substantial removal of carrier density at the Spiro-OMeTAD-perovskite interface within 3 ns via selective charge extraction or via any additional surface recombination. This conclusion can be drawn because in all cases carriers were either generated next to the Spiro-OMeTAD interface, or would have diffused to the interface within the 3-ns window, as evidenced by the fullerene measurements. Thus we have established that the rates for extraction and surface recombination at the Spiro-OMeTAD-perovskite interface must be low, such that the effective lifetime is close to the bulk lifetime. This is in agreement with the lifetimes from time-resolved PL, discussed further in Sec. III D.

4. Transient absorption of perovskite-CTL bilayers

An additional factor complicating the interpretation of OPTP spectroscopy of selective carrier extraction is that $S(t)$ for OPTP is proportional to the sum of the photoconductivity of electrons and holes, and their carrier mobilities may differ. Therefore, extraction of one carrier type may cause a different reduction in $S(t)$ than removal of the other type. Computational studies have suggested similar effective masses for both electrons and holes [31], but the ratio of their mobilities is harder to determine as mobility depends on the scattering rate as well. Therefore, to check that the lack of decay over 3 ns for the Spiro-OMeTAD bilayers was not due to OPTP being less sensitive to hole density (if it were the case that $\mu_h \ll \mu_e$), white light TA spectroscopy was additionally performed, as reported in Fig. 4. In TA spectroscopy $S(t) = \Delta OD$, the change in optical density. The strength of the ground-state bleach [negative ΔOD , red in Fig. 4(a)] of the interband transition can be assumed to be proportional to the carrier density injected, independently of the mobility. Here, experiments were performed at low enough pump fluences that the hot phonon bottleneck regime [28] was not reached, and carriers cooled quickly (within a few picoseconds) to the band edge. The TA dynamics [Fig. 4(b)] show the same trends as for OPTP, with no decay for the Spiro-OMeTAD bilayers over 3 ns, and the fullerene bilayers did exhibit additional decay in comparison with the bare perovskite reference (the amplitudes are not interpreted since they were not as well controlled). The agreement between TA and OPTP transients additionally confirms that the decay of the photoconductance signal is due to carrier removal rather than changes in mobility.

III. CARRIER DYNAMICS MODELING

We developed a theoretical model of the evolution of the charge density within a CTL-perovskite bilayer in order to simulate the dynamical signal $S(t)$ observed in experiments, and to disentangle the different contributions to $S(t)$ from diffusion within the perovskite, population transfer to the CTL, and recombination at the perovskite-CTL interface. A selective interface will clearly lead to the spatial separation of electrons and holes, and the resulting Coulombic forces will influence the motion of carriers within the perovskite (i.e., introducing drift transport in addition to diffusive motion). A mathematical description of $n(x, t)$ and $p(x, t)$ requires solving the nonlinear continuity equations for electrons and holes, including drift and diffusion current terms, along with the electric field $E(x, t)$ obtained from Gauss's law. Krogmeier *et al.* [32] simulated the carrier dynamics of perovskite-CTL bilayers and suggested the importance of Coulombic forces at high carrier densities, such as used in the OPTP and TA experiments reported here. They focused on modeling

the dynamics measured by time-resolved photoluminescence spectroscopy (TRPL) over tens of nanoseconds; here we instead focus on carrier dynamics on the sub-nanosecond timescales relevant to OPTP and TA measurements. Although device simulation packages are available [33,34], these are not designed for simulating the transients of bilayers on picosecond timescales, following pulsed illumination.

A. Numerical model

As described in Appendix D and the Supplemental Material [17], in the present work we developed a numerical solution using the Scharfetter-Gummel discretization of the drift-diffusion current equations and the forward Euler method [35], for parameters that match our experimental conditions. Perovskites are at most weakly doped [36], and hence at the fluences used in OPTP and TA spectroscopy only the photoexcited carriers, n_e, p_e , are considered in the model, as these will have higher density than the equilibrium carriers, n_0, p_0 (i.e., high-level injection $n_e, p_e \gg n_0, p_0$). Experiments were performed at low pump fluences ($0.6\text{--}1.4 \times 10^{17}$ photons per square meter per pulse) such that the OPTP and TA decay curves were flat for the bare perovskite sample (see Figs. 3 and 4), indicating that the fraction of the carrier population that recombined during the measurement window of 3 ns was negligible. Thus recombination within the perovskite can be excluded, which significantly simplifies the interpretation of the data and reduces the number of free parameters in the model. Further, the low fluence allowed the influence of photon reabsorption [37,38] to be ignored in our model as the rate of bimolecular radiative recombination was minimized. The migration of ions is too slow to occur during the measurement window of a few nanoseconds so can be ignored.

The physical processes involved in the simulation are described in Figs. 5(a)–5(c) for the case of electron removal via population transfer to the ETL, under excitation with an initial sheet carrier density of 10^{17} m^{-2} and a penetration depth of 35 nm. Initially, the electrons and holes have the same profile in the perovskite [schematically shown in Fig. 5(a)], while at later times charges can either diffuse away from the interface into the perovskite, or be extracted to the ETL. For a selective ETL we assumed that interfacial electrons were extracted at a rate defined by the interfacial extraction velocity, S , while hole extraction was forbidden. The preferential extraction of electrons into the ETL [Fig. 5(b)] attracts holes in the perovskite towards the interface, and repels electrons, forming an electrical double layer. Further, in the simulation we considered two processes that can reduce the net charge in the ETL [Fig. 5(c)]: (i) cross-interface recombination, where an electron in the LUMO of the ETL recombines with a hole in the VB of the perovskite at a rate

$k_{\text{inter}} n_{\text{CTL}} p(x=0)$, or (ii) hole transfer from the perovskite VB to the HOMO of the ETL with velocity S_{holes} . This later process may be possible given the tail in the density of states for fullerene molecules above their HOMO level, suggesting that the VB offset between fullerene and perovskite is not very large and thus hole extraction may not be blocked very effectively [39]. Cross-interface recombination and hole extraction are difficult to distinguish, as both lead to the loss of a hole from the perovskite and reduce the negative charge in the ETL (they are compared in Supplemental Material [17], Section 2.5).

The results of the simulations are shown in Figs. 5(d)–5(f). As well as plotting the perovskite photoconductance versus pump-probe delay, the decay rate can be conveniently parameterized by the instantaneous lifetime, $\tau^*(t) = -\Delta\sigma/[d(\Delta\sigma)/dt]$. It should be noted that this represents the decay lifetime for the perovskite’s entire sheet carrier density and is thus effected by the distribution of carriers. For example, even if the rate constant for carrier loss at an interface is fixed, the decay rate of the sheet density is faster if carriers are concentrated near the interface, and lower if they are spread throughout the thickness (the green lines, which will be discussed below, are an example of this).

Figure 5(d) shows simulations of the photoconductance $\Delta\sigma$, for an extraction velocity $S = 90 \text{ m s}^{-1}$ and for various cross-interfacial recombination rates, under either front excitation (thick lines) or back excitation (thin lines). Considering first the case without cross-interfacial recombination, $k_{\text{inter}} = 0$ (blue lines), for front excitation the simulated photoconductance of the perovskite initially decays before plateauing (thick line), while for back excitation the photoconductance only appreciably decays after about 1 ns (thin line). The plateaux in the photoconductance corresponds to a rapidly increasing τ^* [blue line, Fig. 5(e)], and can be understood as resulting from the formation of the electrical double layer: the Coulomb repulsion of electrons away from the interface prevents further electron extraction, leading to the population decay rate slowing. The electrical double layer’s formation can be seen from the excess electron sheet density in the CTL, as reported in Fig. 5(f). The electron sheet density in the CTL can be seen to rapidly rise within 200 ps to above 10% of the initial sheet carrier density in the perovskite, before rolling over as the extraction rate slows.

In line with the findings of Ref. [32], simulations for carrier sheet densities three orders of magnitude lower (10^{14} rather than 10^{17} m^{-2}) do not show such a Coulombic bottleneck for extraction (see Supplemental Material [17], Fig. S22). To verify the robustness of the observed plateau in the simulated transients with $k_{\text{inter}} = 0$ (blue lines), we performed alternative simulations whereby electrons were allowed to be extracted from deeper into the perovskite layer (smearing the interface), or the perovskite’s permittivity was increased to reduce the electric field

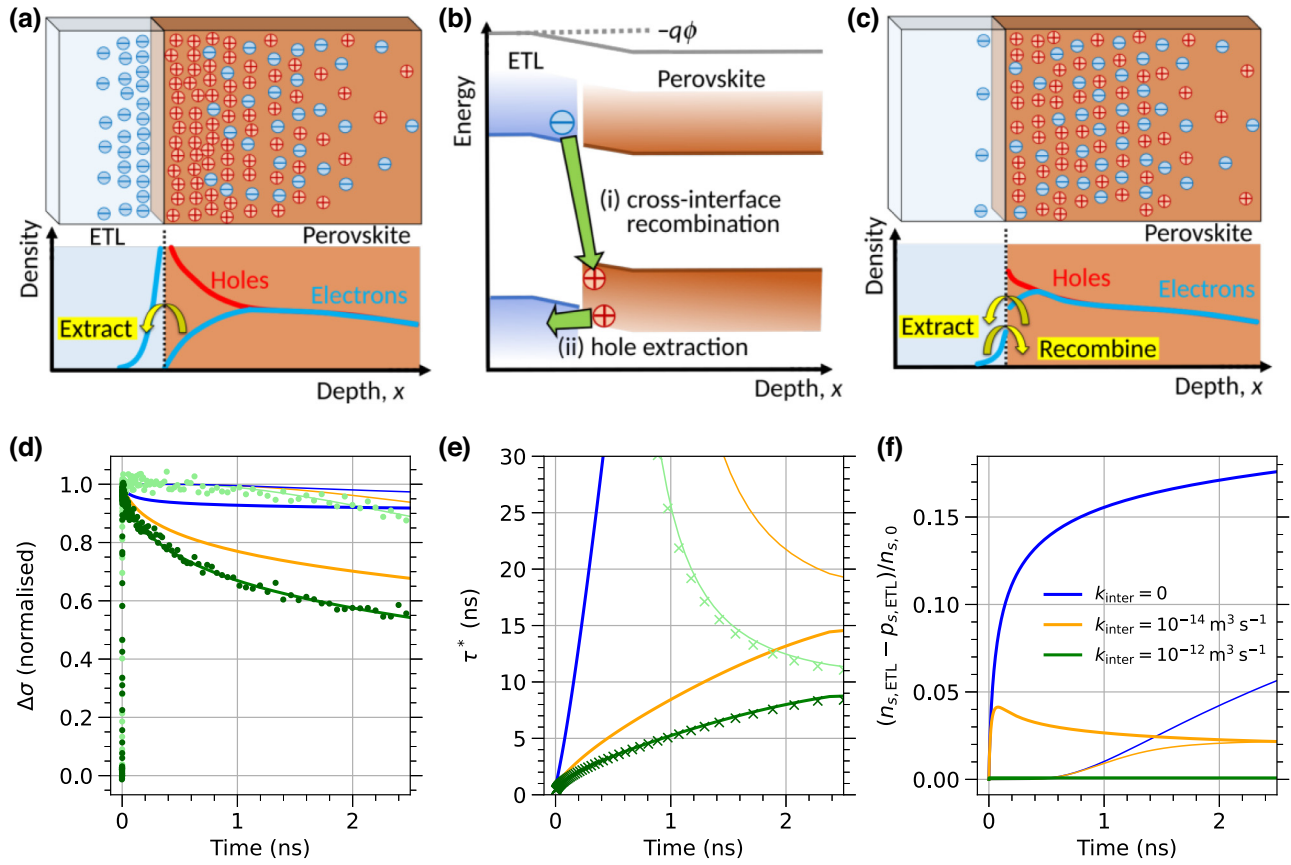


FIG. 5. (a) Schematic of charge distribution in a perovskite-ETL bilayer around 100 ps after photoexcitation through the ETL, without interface recombination. Electrons (blue) have been extracted into the ETL (gray), and an excess of holes (red) has built up in the perovskite near the interface, forming an electric double layer. (b) Schematic band diagram at the interface showing processes that lower the net charge in the ETL, either (i) an electron in the ETL recombining with a hole in the perovskite, or (ii) a hole moving from the perovskite to the ETL. (c) With strong interfacial recombination the electron density in the CTL is lower than that in (a), and the net charge difference in the perovskite near the interface is smaller. (d) Simulated transient photoconductance $\Delta\sigma$ when photoexcited on the front (thick lines) or back (thin lines), either without interfacial recombination (blue), or with $k_{\text{inter}} = 10^{-14} \text{ m}^3 \text{ s}^{-1}$ (orange) or $k_{\text{inter}} = 10^{-12} \text{ m}^3 \text{ s}^{-1}$ (green), for an extraction velocity $S = 90 \text{ m s}^{-1}$. Points show the experimental data from Fig. 3(c), for the perovskite- C_{60} bilayer. (e) Effective lifetime $\tau^*(t) = -\Delta\sigma/[d(\Delta\sigma)/dt]$ calculated for the curves shown in (d), indicating that the decay rate changes dynamically with pump-probe delay. Crosses indicate results from the analytical model with $S = 90 \text{ m s}^{-1}$ and $\mu = 15 \text{ cm}^2 \text{ V}^{-1} \text{ s}^{-1}$. (f) The excess sheet charge density in the ETL, $n_{s,\text{ETL}} - p_{s,\text{ETL}}$, shown normalized by the initial sheet charge density in the perovskite $n_{s,0} = 1 \times 10^{13} \text{ cm}^{-2}$.

strength (see Supplemental Material [17], Figs. S20 and S21). However, even extreme smearing of the interface or extreme permittivity values were not sufficient to remove the plateau.

The simulations with $k_{\text{inter}} = 0$ described above are qualitatively different from the experimental $S(t)$ observed for the fullerene bilayers: the experiments did not show a plateau after a rapid decay, rather the OPTP, TA and TRPL exhibited a continual decay. Hence, we can conclude that there is a physical process that prevents the formation of the Coulomb bottleneck for extraction, such as cross-interface recombination or hole extraction. When cross-interface recombination was included by setting $k_{\text{inter}} = 10^{-14} \text{ m}^3 \text{ s}^{-1}$ [orange lines in Figs. 5(d)–5(f)] the

photoconductance continually decreased with time, and the extraction rate does not slow significantly. This is a result of the cross-interface recombination reducing the strength of the Coulomb bottleneck: the excess sheet density in the ETL initially increases [Fig. 5(f), orange line], but the accumulation of both $p(x=0)$ and the electron density in the ETL causes the cross-interfacial recombination rate to increase until it balances the extraction rate, meaning the net charge in the ETL stops rising and the Coulomb bottleneck is weak. When the cross-interfacial recombination rate balances the extraction rate, extracted electrons can be considered to immediately undergo recombination. With an even higher rate $k_{\text{inter}} = 10^{-12} \text{ m}^3 \text{ s}^{-1}$ no substantial charge density builds up in the ETL at all

[green lines in Fig. 5(f)]. In this case, τ^* increases slowly due to carriers diffusing away from the interface (alluded to earlier), rather than the Coulombic bottleneck. Figure 5(d) shows that parameter values of $S = 90 \text{ m s}^{-1}$ and $k_{\text{inter}} = 10^{-12} \text{ m}^3 \text{ s}^{-1}$ give excellent agreement with the experimental data.

Summarizing the results from the numerical simulation, the relative amplitude of the extraction and cross-interfacial recombination rate constants can be qualitatively obtained by visually inspecting the shape of the experimental decay at delay times below a few nanoseconds. For Spiro-OMeTAD, population removal (extraction to the HTL or recombination) was not observed on timescales of 1 ps to 3 ns, and hence the extraction velocity S and surface recombination are small. For the fullerenes, the decay of the population within 3 ns indicates that the charge extraction rate was higher, and the persistence of the decay over 3 ns indicates that interfacial removal/loss processes, such as cross-interface recombination or hole extraction, limit the formation of a Coulomb bottleneck. In the following sections we quantify the extraction velocity S and k_{inter} .

B. Analytical “one-step” model

In the limiting case of rapid cross-interfacial recombination or simultaneous extraction of both carriers (such as for fullerene bilayers), we now discuss a simpler theoretical model of the carrier dynamics with fewer free parameters than the numerical model. With rapid cross-interfacial recombination, the two-step process of extraction then recombination is effectively a one-step process limited by the slowest step: extraction. Therefore, this effective surface recombination has a velocity given by the extraction velocity. This process means the electron and hole densities at the interface remain similar, and the carrier removal rate becomes proportional to the electron density in the perovskite at the interface. This scenario satisfies the neutrality approximation, $n(x) = p(x)$, so there is no need to solve Gauss’s law and the two continuity equations can be combined into a single equation for the balanced density $n(x) = p(x)$ [40]. For high-level injection, this ambipolar continuity equation is just the diffusion equation, and if the effective surface recombination is linear in density, then the equation can be solved analytically by separation of variables [41]:

$$n(x, t) = e^{-t/\tau_B} \sum_{m=1}^{\infty} A_m \cos(\alpha_m(L - x)) e^{-\alpha_m^2 D t} \quad (1)$$

where τ_B is the bulk recombination time in the perovskite and the α_m are the different eigenvalue solutions of the transcendental equation $\alpha_m \tan(\alpha_m L) = S/D$ (see Supplemental Material [17], Section 2.3). Hence, the α_m depend on L , S , and D , where the surface recombination velocity S is equal to the electron extraction velocity used in

the numerical model, and D is the *ambipolar* diffusion coefficient. The Fourier coefficients, A_m , are determined by the initial distribution and therefore by the absorption coefficient at the pump wavelength (from UV-visible spectroscopy). Similar expressions have been used to analyze surface recombination in silicon [22,42,43], where D and L are substantially larger than in perovskites. In order to compare the simulated sheet densities [an even simpler Fourier series than Eq. (1)] with the measured $S(t) = -\Delta T/T$ we used the standard thin-film expression [44]. Overall, the only free parameters in the model were the ambipolar diffusion coefficient, D , and the interfacial extraction velocity, S . Using this expression with $S = 90 \text{ m s}^{-1}$ and $\mu = 15 \text{ cm}^2 \text{ V}^{-1} \text{ s}^{-1}$ (or $D = 0.39 \text{ cm}^2 \text{ s}^{-1}$) yields $\tau^*(t)$ shown by the green points reported in Fig. 5(e), which are almost identical to the numerical simulation’s results (solid green lines) for the same parameters.

At late times, the instantaneous lifetime tended to a constant, namely $\tau^*(t \rightarrow \infty) \rightarrow 10 \text{ ns}$ in the case shown in Fig. 5(e), and was similar for both front and back excitation. In this limit of long time delays, the carrier distribution described by Eq. (1) is dominated by the smallest eigenvalue α_m , because it has the slowest temporal decay (and also has the smoothest spatial distribution). The distribution becomes stationary: the shape does not change, only the amplitude alters, which decays with rate $1/\tau_{\text{eff}} = 1/\tau_B + 1/\tau_S$, where $1/\tau_S = \alpha_0^2 D$ and τ_B is the bulk recombination lifetime. For a semiconductor with large S on one surface (the extraction layer here), and negligible S on the other surface, τ_S can be approximated as [43]

$$\tau_s = \frac{L}{S} + \frac{4}{D} \left(\frac{L}{\pi} \right)^2. \quad (2)$$

In contrast to representing surface recombination, as witnessed in a single semiconductor [43], here for the perovskite-CTL bilayer S represents extraction at speed S followed by fast cross-interface recombination. The second term in τ_s accounts for the time required for charges to diffuse through the film’s thickness before reaching the interface. Calculating the surface lifetime using Eq. (2) for the same parameters as the numerical and analytical simulations in Fig. 5 (i.e., $L = 600 \text{ nm}$, $S = 90 \text{ m s}^{-1}$, $D = 0.39 \text{ cm}^2 \text{ s}^{-1}$) yields $\tau_s = 10.5 \text{ ns}$ and thus $\tau_{\text{eff}} = 10.0 \text{ ns}$, in excellent agreement with $\tau^*(t \rightarrow \infty)$ deduced from the models.

C. Global fits to experiment

As an analytical expression, Eq. (1) can be fitted iteratively to the experimental data orders of magnitude faster than the full numerical solution. By globally fitting a set of decay curves for different experimental conditions, using a common set of parameters, one can obtain a sharper minimum of the global cost function with respect to the

free parameters than is possible for a fit to just a single decay curve. Here, including front and back excitation with a short penetration depth gave a strong constraint on the ambipolar D (and mobility), as the shape of the decay is strongly influenced by the time taken for carriers to diffuse through the perovskite to the CTL interface. It is important to note that because the ambipolar continuity equation is linear, the normalized decay shape is the same regardless of the sheet density, and any error in the estimation of the initial sheet density has no impact on the parameters deduced.

Figure 6 shows that the global fits of the analytical model (solid lines) accurately reproduce all the features of the OPTP experiments (points), with small residual error (a map of the residual versus μ and S for the C_{60} bilayer contains a single minimum, as shown in Supplemental Material [17], Fig. S23). The experimental measurement for the C_{60} bilayer with 410-nm excitation showed a clear delay in the decay of the signal when exciting on the back (quartz) side, which was captured by the model. The values of the best-fit parameters were an ambipolar mobility $\mu = 15 \pm 0.6 \text{ cm}^2 \text{ V}^{-1} \text{ s}^{-1}$ (or ambipolar $D = [3.8 \pm 0.2] \times 10^{-5} \text{ m}^2 \text{ s}^{-1}$) and $S = 90 \pm 2 \text{ m s}^{-1}$.

Returning to the more detailed two-step numerical model, for the C_{60} bilayers we performed a series of simulations for different values of S and k_{inter} in order to estimate the values of the two rate constants. In Fig. 6(b) the rms error between the data reported in Fig. 6(a) (the fitted analytical solution) and the numerical model is shown as a function of both extraction velocity S and the cross-interfacial recombination rate k_{inter} . The numerical simulation best agrees when the rms error is close to zero (white area), inside the area defined by the black contour,

corresponding to the region around $S = 90 \text{ m s}^{-1}$ and $k_{\text{inter}} \geq 7 \times 10^{-13} \text{ m}^3 \text{ s}^{-1}$. The contour plot shows a single minimum, but the contours extend towards large values of k_{inter} , indicating this is a lower bound for k_{inter} . The surface recombination velocity in the one-step model is equivalent to the extraction velocity in the two-step model (both are 90 m s^{-1}).

For the PCBM bilayers, while the decay under back excitation was slower compared with excitation on the front (PCBM) side, it did not show a distinct delay to the start of the decay. This suggests the solution-deposited PCBM had penetrated into the perovskite's grain boundaries, and that the planar bilayer model may oversimplify a more complex scenario for the PCBM bilayer. Alternatively, the solution-phase processing to add the PCBM may have modified the strain and/or defect density in the perovskite, changing its τ_B . However, a global fit to measurements on PCBM yielded reasonable fits [Fig. 6(c)], with best-fit parameters $\mu = 15 \pm 1 \text{ cm}^2 \text{ V}^{-1} \text{ s}^{-1}$, $S = 55 \pm 2 \text{ m s}^{-1}$, and $\tau_B = 15 \pm 2 \text{ ns}$. Therefore we conclude that the electron extraction velocities for PCBM is $S \simeq 55 \text{ m s}^{-1}$, slightly smaller than $S = 90 \pm 2 \text{ m s}^{-1}$ for the C_{60} bilayer. We note that Krogmeier *et al.* [32] deduced a value of $S = 53 \text{ m s}^{-1}$ for a perovskite-PCBM bilayer from the power dependence of their PL dynamics on nanosecond timescales, very similar to our values.

D. Further discussion

By considering the results obtained from the numerical model including the Coulombic forces and interfacial recombination, we demonstrated that the accumulation of electrons in the fullerene layer is undermined by processes

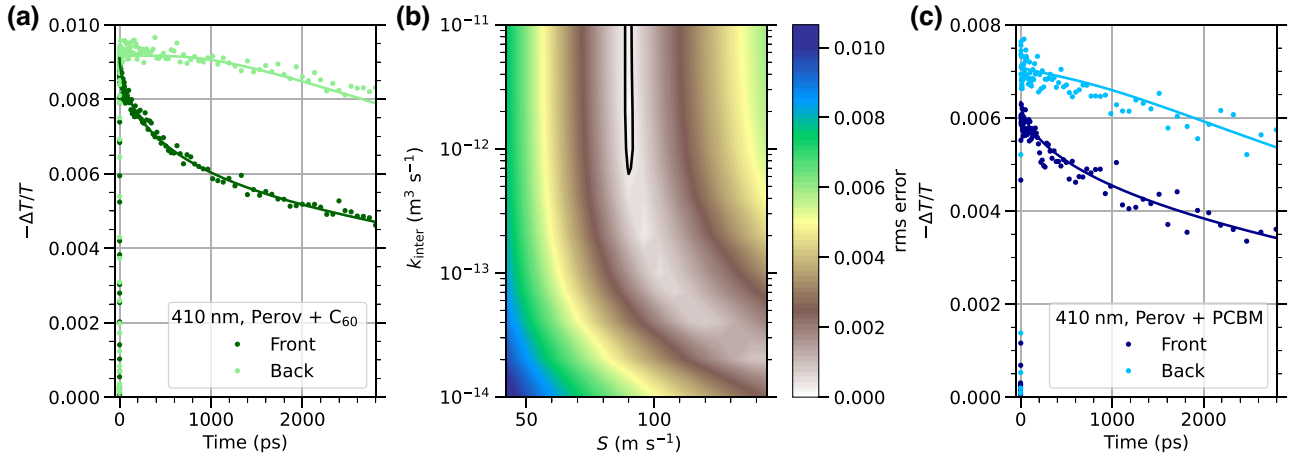


FIG. 6. (a) Experimental OPTP results for perovskite- C_{60} bilayer (points) under front and back excitation at 410 nm, along with fits from the analytical model (solid lines) with $S = 90 \text{ m s}^{-1}$, $\mu = 15 \text{ cm}^2 \text{ V}^{-1} \text{ s}^{-1}$, and $\tau_B = 200 \text{ ns}$. (b) Root-mean-square (rms) error determined from the residuals between the numerical simulation and the analytical fit to the data in (a), for $\mu = 15 \text{ cm}^2 \text{ V}^{-1} \text{ s}^{-1}$ and different values of S and k_{inter} . The black contour illustrates the global minimum error, which occurs at $S = 90 \text{ m s}^{-1}$, and $k_{\text{inter}} \geq 10^{-12} \text{ m}^3 \text{ s}^{-1}$. (c) Experimental results for perovskite-PCBM bilayers (points) under front and back excitation, along with fits from the analytical model (solid lines) with $S = 55 \text{ m s}^{-1}$, $\mu = 15 \text{ cm}^2 \text{ V}^{-1} \text{ s}^{-1}$, and $\tau_B = 15 \text{ ns}$.

such as cross-interface recombination or hole extraction. This corroborates the interpretation of the SS-PL measurements [Fig. 2(e)] in which PL quenching by the fullerenes is interpreted as resulting from the introduction of additional channels for nonradiative recombination [18–20]. Cross-interface recombination and hole extraction are difficult to distinguish, as both lead to the loss of a hole from the perovskite and reduce the negative charge in the ETL (they are compared in Supplemental Material [17], Section 2.5). Both mechanisms have been discussed in the literature. Schulz *et al.* [39] suggested that the observed tail of states above the C_{60} VB, reduces the energy offset between the C_{60} and the perovskite VBs and thus may allow some hole extraction into the ETL. In contrast, Warby *et al.* [45] concluded that cross-interface recombination is dominant. They observed that adding a C_{60} layer increased the subgap feature in the external quantum efficiency (EQE), indicating the presence of intragap states. They did not observe any PL or electroluminescence from the C_{60} layer, which could be expected following hole extraction and subsequent radiative recombination within the C_{60} . Therefore, they proposed recombination is mostly cross-interface via intragap states or broadening of the C_{60} LUMO states due to disorder, which was previously reported [46]. The attribution to cross-interface recombination is further supported by the observation that adding a LiF interlayer a few nanometers thick between the perovskite and C_{60} can reduce the subgap feature in EQE (i.e., lower the intragap state density) and improve V_{oc} . Liu *et al.* [47] also showed that nanometer-thick interlayers improved the performance. Their density functional theory simulations showed that when C_{60} is close to the perovskite surface, new states form in the bandgap, but this does not occur if the C_{60} is moved away by an interlayer.

Finally, regarding the Spiro-OMeTAD-perovskite interface, Eq. (2) can be used to roughly estimate the surface loss or removal velocity from the PL lifetime. The PL data in Fig. 2(g) show that the effective lifetime of the Spiro-OMeTAD bilayer (about 100 ns) is roughly half that of the perovskite bulk (estimated from the bare perovskite reference), meaning that the surface lifetime is comparable to the bulk lifetime, $\tau_s \approx \tau_B \approx 200$ ns. Since the second term (i.e., the diffusion contribution) in the surface lifetime [Eq. (2)] is only approximately 3 ns, the surface lifetime is dominated by the first term $\tau_s \approx L/S$. Therefore, we estimated $S \approx 2$ m s⁻¹, more than an order of magnitude below the surface extraction rate for the ETL bilayers. With no rapid extraction for the HTL, it was not possible to determine the cross-interfacial recombination rate from the comparison between ultrafast spectroscopy and numerical simulation.

IV. CONCLUSION

The combination of picosecond optical spectroscopy and an advanced carrier dynamics model that includes

Coulombic forces allowed us to provide an improved understanding of the charge carrier dynamics in perovskite-CTL bilayer heterostructures that employ three of the most common CTLs, namely C_{60} , PCBM, and Spiro-OMeTAD. For perovskite-Spiro-OMeTAD bilayers, negligible decay of the carrier density in the perovskite was observed within the first 3 ns after photoexcitation, indicating that hole extraction was relatively slow (extraction velocity $S \approx 2$ m s⁻¹) compared with the faster electron extraction velocity of the fullerenes ($S \approx 55$ m s⁻¹ for PCBM and $S \approx 90$ m s⁻¹ for C_{60}). Importantly, surface recombination at the interface must also be slow, which may explain the excellent performance of Spiro-OMeTAD in solar cell devices despite its relatively slow hole extraction. For perovskite-fullerene bilayers, when charge carriers were photoexcited near the fullerene interface, the carrier density decayed within the first few hundred picoseconds and continued to decay on nanosecond timescales. The numerical model including Coulombic forces indicated that at the higher carrier densities used in pump-probe experiments, the population decay should plateau within the first nanosecond due to the accumulation of extracted electrons in the fullerene repelling electrons in the perovskite to form an electrical double layer. The absence of this characteristic fingerprint of a Coulombic bottleneck indicates that there is substantial loss of holes at the interface. We highlighted cross-interface recombination and hole extraction as possible physical mechanisms active at the interface, but note that these cannot be distinguished by these experiments.

The numerical and analytical carrier dynamics models presented were found to accurately replicate the experimental data, and determined the interfacial extraction velocity, along with the ambipolar diffusion coefficient for vertical transport through the perovskite films. Perovskite-fullerene bilayers were found to fall under the limiting case of rapid interfacial recombination (for which the analytical “one-step” model is suitable), and thus only a lower bound for the cross-interface recombination rate constant can be determined.

The trends observed with subnanosecond terahertz and transient absorption measurements were also observed for nanosecond photoluminescence measurements that use lower injected carrier densities which are comparable to solar illumination, indicating that the properties extracted from the subnanosecond measurements using higher injected carrier densities are relevant to operational carrier densities.

Having identified targets for improvement in three of the most popular CTLs, future work will build upon the combination of picosecond optical spectroscopy and drift-diffusion modeling presented here, for instance to study the interface extraction and recombination kinetics of other heterojunctions, or to fully elucidate the interfacial recombination processes active at such interfaces.

ACKNOWLEDGMENTS

E.B.C. would like to thank the EPSRC (UK) for a PhD studentship. R.J.M. would like to acknowledge funding from the EPSRC (EP/V001302/1). K.D.G.I.J. thanks the Equal Opportunities Foundation (Hong Kong) for financial support. The authors thank Prof. Ross Hatton, Stephen York and Dr. Eric Hu for assistance with C_{60} film deposition, SEM and AFM studies, respectively. The authors acknowledge use of the Warwick Centre for Ultrafast Spectroscopy Research Technology Platform.

APPENDIX A: MATERIAL SYNTHESIS

In this work, thin films of $(FA_{0.83}MA_{0.17})_{0.95}Cs_{0.05}Pb(I_{0.83}Br_{0.17})_3$ were investigated. All processing was carried out in a N_2 glove box with both O_2 and H_2O levels below 0.1 ppm. Similar results were obtained on films of $(FA_{0.83}MA_{0.17})_{0.95}Cs_{0.05}PbI_3$. Perovskite precursors were prepared such that the (FA + MA):Pb molar ratio was 1 : 1.1 for both compositions. For the mixed I-Br composition, PbI_2 (1.1 mmol, TCI) was added to a DMF:DMSO mix (1 ml, 4 : 1 ratio by volume), followed by FAI (1 mmol, Greatcell solar), $PbBr_2$ (0.22 mmol, TCI), and then MABr (0.2 mmol, Greatcell Solar). A CsI solution was prepared by dissolving CsI (78 mg, Sigma Aldrich) in DMSO (200 μ l). This solution (42 μ l) was added to the $PbI_2 + FAI + PbBr_2 + MABr$ in DMF/DMSO mix.

For the Spiro-OMeTAD layer, Spiro-OMeTAD (72.3 mg, Borun) was dissolved in chlorobenzene (CB). Separately, a solution of FK209 in acetonitrile (300 mg ml^{-1}) and a solution of Li-TFSi in acetonitrile (520 mg ml^{-1}) were prepared. To the Spiro solution, tBP solution (28.8 μ l), Li-TFSi solution (17.5 μ l) and FK209 solution (29 μ l) were added. For PC₆₀BM, powder (20 mg, Nano-C) was dissolved in CB (1 ml).

To make thinner perovskite films, the perovskite solution (100 μ l) was added to the DMF:DMSO 4 : 1 mix (500 μ l). For the thinner CTLs, the Spiro-OMeTAD (50 μ l) and PCBM solutions were added to CB (150 μ l).

The perovskite layers were formed by spin-coating on quartz substrates using an anti-solvent method. The perovskite solution was dropped onto the substrate prior to spinning. The spinning was divided into two steps. First, the substrate was accelerated up to 1000 rpm at a rate of 200 rpm/s, then accelerated after 8 s to 6000 rpm at a rate of 1000 rpm/s. Next, 150 μ l of CB was dropped onto the spinning substrate 30 s into the second step. The sample was then annealed at 100 °C for 1 h.

To form the Spiro-OMeTAD layer, the perovskite sample was accelerated to 4000 rpm at a rate of 2000 rpm/s, and the Spiro-OMeTAD solution was dropped onto the spinning perovskite sample 5 s after starting (spinning stopped at 25 s). To form the PCBM layer, the PC₆₀BM solution was dropped onto the stationary perovskite sample, which was then accelerated to 1000 rpm at a rate of

1000 rpm/s (spinning stopped at 30 s). The C_{60} layers were deposited by thermal evaporation at a rate of 0.1–0.4 $\text{\AA} s^{-1}$.

Top-down scanning electron microscope images were recorded with a Zeiss SUPRA 55-VP, and cross-sectional images were taken with a Zeiss Gemini 500.

APPENDIX B: STEADY-STATE OPTICAL AND TIME-RESOLVED PL SPECTROSCOPY

UV-visible spectroscopy was performed using a spectrophotometer (Perkin Elmer Lambda 1050) with an integrating sphere module, to determine the film's absorbance taking account of scatter and reflection losses. The steady-state (SS) and time-resolved (TR) PL were measured using a Horiba Jobin Yvon Fluorolog-3 fluorescence spectrometer, comprising a iHR320 monochromator and a Hammamatsu R982P PMT. TR-PL was measured by time-correlated single photon counting (TCSPC), with the timing electronics provided by a Horiba FluoroHub. The samples were illuminated with pulsed diode sources with center wavelengths of 405 nm and 633 nm, pulse energies of approximately 3.4 and 1.7 pJ/pulse respectively, and pulse duration less than 200 ps. The angle of incidence was approximately 45° and the Gaussian illumination spots yielded maximum pulse fluences of 25 and 10 $nJ cm^{-2}$ per pulse (5×10^{14} and 3×10^{14} photons per square meter per pulse) for 405 nm and 633-nm excitation, respectively. The PL was collected at 45°. A long pass filter was placed between the sample and the spectrometer, and the spectrometer was set to detect at the peak of the PL spectrum (760 nm). The fraction of photoexcitation cycles that resulted in detection of a photon (called count rate) was kept below 2%. The PL decays were much longer than the instrument response function (IRF, 2 ns), and so iterative deconvolution of the data and the IRF was not necessary. The repetition period of the pulsed diodes was chosen to ensure the PL intensity decayed to zero before the next pump pulse arrived (typically 1–10 μ s). To normalize the TCSPC decays, the background offset was first subtracted, and then the data were normalized to a value just after the initial small spike resulting from residual scatter of the pump light.

The relatively low fluence resulted in a low carrier density injection into the perovskite, and carrier recombination was therefore dominated by defect-mediated recombination [48], which is thus sensitive to changes in the defect density due to illumination or atmosphere [49–52]. The TCSPC decay profile can thus depend on the environmental exposure of the sample and may change during an experimental session. To study the differences between the CTLs we adopted an experimental protocol that minimized any differences in surface defect density during measurements. Samples were measured in ambient air starting after several minutes of exposure, until the PL lifetime had stabilized, so that all samples had the opportunity to reduce

their surface defect density to a similar level. This resulted in bright, long-lived PL dynamic data that reproduced when repeatedly measured, making differences due to the CTL easier to distinguish. Alternative environments (e.g., nitrogen) resulted in shorter PL lifetimes, which makes differences due to CTLs harder to distinguish.

APPENDIX C: ULTRAFAST SPECTROSCOPY

Time-resolved measurements of carrier densities were performed using transient absorption (TA) spectroscopy and optical pump terahertz probe (OPTP) spectroscopy, which measured dynamics with subpicosecond resolution and over a 3-ns range. The OPTP setup is described in detail in Ref. [29]. Photon fluxes per pulse for OPTP and TA were calculated by considering the effective area of the overlapping pump and probe spots. For TA, the Gaussian intensity profile of the pump and probe spots had $\sigma \sim 0.4$ mm and $\sigma \sim 0.04$ mm, respectively. For OPTP, the Gaussian profile of the pump and probe spots had $\sigma \sim 1$ mm and $\sigma \sim 0.4$ mm, respectively (for terahertz this was the standard deviation of the electric field).

For TA, femtosecond laser pulses were generated by a Spitfire Ace amplified Ti:Sapphire laser system (Spectra Physics), outputting 13 mJ pulses with a center wavelength of 800 nm at a repetition rate of 1 kHz. A beam splitter directed a fraction of this beam power for use in the TA experiment (another fraction was used for OPTP experiments). A second beam splitter directed a fraction of this beam power to an optical parametric amplifier (Light Conversion TOPAS) to generate pump pulses of different wavelengths, and the other fraction of the beam was focused into a 2-mm CaF₂ window to generate a white light continuum (the window is continuously translated to prevent damage). A mechanical delay stage was used to vary the path length of the beam that generates the white light pulse, and thus vary the relative time delay between the white light pulse and pump pulse arriving at the sample. A mechanical chopper (500 Hz) was used to alternately block and pass the pump pulse, resulting in the white light pulses alternately measuring pump-on and pump-off conditions. The white light pulses were directed into a fibre coupled Avantes spectrometer (Avaspec 1650 Fast USB) consisting of a grating and a multipixel CCD, to measure the spectra shot-by-shot. ΔOD spectra were calculated from pairs of pump-on and pump-off spectra.

APPENDIX D: THEORETICAL METHODS

The numerical solution to the coupled continuity and Poisson equations was constructed in Python with calculations accelerated by the Numba library. The coupled equations were solved using the Forward Euler method, and the drift-diffusion equations for current were discretized using the Scharfetter-Gummel scheme to improve stability [35]. The drift-diffusion expression for the electron charge

current is

$$J_n(x, t) = -q\mu_e n(x, t) \frac{\partial \Phi(x, t)}{\partial x} + qD_e \frac{\partial n(x, t)}{\partial x} \quad (\text{D1})$$

and includes the mobility μ_e , the diffusion coefficient D_e , the electric potential Φ and the electron density n . A similar expression holds for holes. The electron and hole diffusion constants were given by $D_{e,h} = \mu_{e,h} k_B T / q$ for mobilities $\mu_{e,h}$. Here we assumed equal electron and hole mobilities in the perovskite for simplicity. The mobility of carriers in the CTL is much lower than that of the perovskite, and it was thus assumed that any carriers extracted into the CTL would remain close to the interface within the 3 ns time window of the experiments, and hence that all CTL carriers contribute to cross-interface recombination. Poisson's equation, $\partial^2 \Phi(x, t) / \partial x^2 = -\rho_f(x, t) / \epsilon_r \epsilon_0$, was solved at each time step for free charge density ρ_f , where the perovskite layer was assumed to have dielectric constant $\epsilon_r = 20$. Numerical simulations were validated by checking numerical convergence for a variety of discretization conditions, and by comparison with analytical results in limiting cases (see Supplemental Material [17], Figs. S12–S16) The results presented here used a 3-nm spatial step, and a 10-fs time step over the 2.5-ns simulation window. The initial photoexcited carrier density and depth profile in the perovskite matched those used in the experiment.

-
- [1] M. M. Lee, J. Teuscher, T. Miyasaka, T. N. Murakami, and H. J. Snaith, Efficient hybrid solar cells based on meso-structured organometal halide perovskites, *Science* **338**, 643 (2012).
 - [2] A. K. Jena, A. Kulkarni, and T. Miyasaka, Halide perovskite photovoltaics: Background, status, and future prospects, *Chem. Rev.* **119**, 3036 (2019).
 - [3] K. Jayawardena, R. M. I. Bandara, M. Monti, E. Butler-Caddle, T. Pichler, H. Shiozawa, Z. Wang, S. Jenatsch, S. J. Hinder, M. G. Masteghin, M. Patel, H. M. Thirimanne, W. Zhang, R. A. Sporea, J. Lloyd-Hughes, and S. R. P. Silva, Approaching the Shockley-Queisser limit for fill factors in lead-tin mixed perovskite photovoltaics, *J. Mater. Chem. A* **8**, 693 (2020).
 - [4] P. Würfel and U. Würfel, *Physics of Solar Cells: From Basic Principles to Advanced Concepts* (Wiley-VCH, Weinheim, 2009).
 - [5] U. Würfel, A. Cuevas, and P. Würfel, Charge carrier separation in solar cells, *IEEE J. Photovoltaics* **5**, 461 (2015).
 - [6] K. O. Hara and N. Usami, Theory of open-circuit voltage and the driving force of charge separation in pn-junction solar cells, *J. Appl. Phys.* **114**, 153101 (2013).
 - [7] B. Lipovšek, F. Smole, M. Topič, I. Humar, and A. R. Sinigoj, Driving forces and charge-carrier separation in p-n junction solar cells, *AIP Adv.* **9**, 055026 (2019).
 - [8] E. J. Juarez-Perez, M. Wußler, F. Fabregat-Santiago, K. Lakus-Wollny, E. Mankel, T. Mayer, W. Jaegermann, and

- I. Mora-Sero, Role of the selective contacts in the performance of lead halide perovskite solar cells, *J. Phys. Chem. Lett.* **5**, 680 (2014).
- [9] Y. Zhang, M. Liu, G. E. Eperon, T. C. Leijtens, D. McMeekin, M. Saliba, W. Zhang, M. De Bastiani, A. Petrozza, L. M. Herz, M. B. Johnston, H. Lin, and H. J. Snaith, Charge selective contacts, mobile ions and anomalous hysteresis in organic–inorganic perovskite solar cells, *Mater. Horiz.* **2**, 315 (2015).
- [10] J.-F. Liao, W.-Q. Wu, Y. Jiang, J.-X. Zhong, L. Wang, and D.-B. Kuang, Understanding of carrier dynamics, heterojunction merits and device physics: Towards designing efficient carrier transport layer-free perovskite solar cells, *Chem. Soc. Rev.* **49**, 354 (2020).
- [11] C. M. Wolff, P. Caprioglio, M. Stolterfoht, and D. Neher, Nonradiative recombination in perovskite solar cells: The role of interfaces, *Adv. Mater.* **31**, 1902762 (2019).
- [12] V. M. Le Corre, M. Stolterfoht, L. Perdigón Toro, M. Feuerstein, C. Wolff, L. Gil-Escrig, H. J. Bolink, D. Neher, and L. J. A. Koster, Charge transport layers limiting the efficiency of perovskite solar cells: How to optimize conductivity, doping, and thickness, *ACS Appl. Energy Mater.* **2**, 6280 (2019).
- [13] J. J. Yoo, S. S. Shin, and J. Seo, Toward efficient perovskite solar cells: Progress, strategies, and perspectives, *ACS Energy Lett.* **7**, 2084 (2022).
- [14] E. Aydin, T. G. Allen, M. De Bastiani, L. Xu, J. Ávila, M. Salvador, E. Van Kerschaver, and S. De Wolf, Interplay between temperature and bandgap energies on the outdoor performance of perovskite/silicon tandem solar cells, *Nat. Energy* **5**, 851 (2020).
- [15] M. De Bastiani, A. J. Mirabelli, Y. Hou, F. Gota, E. Aydin, T. G. Allen, J. Troughton, A. S. Subbiah, F. H. Isikgor, J. Liu, L. Xu, B. Chen, E. Van Kerschaver, D. Baran, B. Fraboni, M. F. Salvador, U. W. Paetzold, E. H. Sargent, and S. De Wolf, Efficient bifacial monolithic perovskite/silicon tandem solar cells via bandgap engineering, *Nat. Energy* **6**, 167 (2021).
- [16] M. Saliba, T. Matsui, J. Y. Seo, K. Domanski, J. P. Correa-Baena, M. K. Nazeeruddin, S. M. Zakeeruddin, W. Tress, A. Abate, A. Hagfeldt, and M. Grätzel, Cesium-containing triple cation perovskite solar cells: Improved stability, reproducibility and high efficiency, *Energy Environ. Sci.* **9**, 1989 (2016).
- [17] See Supplemental Material <http://link.aps.org/supplemental/10.1103/PhysRevApplied.22.024013> for additional optical data, details of the numerical and analytical models, and additional simulation results. It includes additional Refs. [53–56].
- [18] V. Sarritsu, N. Sestu, D. Marongiu, X. Chang, S. Masi, A. Rizzo, S. Colella, F. Quochi, M. Saba, A. Mura, and G. Bongiovanni, Optical determination of Shockley-Read-Hall and interface recombination currents in hybrid perovskites, *Sci. Rep.* **7**, 1 (2017).
- [19] M. Stolterfoht, C. M. Wolff, J. A. Márquez, S. Zhang, C. J. Hages, D. Rothhardt, S. Albrecht, P. L. Burn, P. Meredith, T. Unold, and D. Neher, Visualization and suppression of interfacial recombination for high-efficiency large-area pin perovskite solar cells, *Nat. Energy* **3**, 847 (2018).
- [20] E. M. Hutter, T. Kirchartz, B. Ehrler, D. Cahen, and E. von Hauff, Pitfalls and prospects of optical spectroscopy to characterize perovskite-transport layer interfaces, *Appl. Phys. Lett.* **116**, 100501 (2020).
- [21] H. Hempel, *et al.*, Predicting solar cell performance from terahertz and microwave spectroscopy, *Adv. Energy Mater.* **12**, 2102776 (2022).
- [22] E. Butler-Caddle, N. E. Grant, S. L. Pain, J. D. Murphy, K. D. G. I. Jayawardena, and J. Lloyd-Hughes, Terahertz photoconductance dynamics of semiconductors from subnanosecond to millisecond timescales, *Appl. Phys. Lett.* **122**, 012101 (2023).
- [23] D. Shi, X. Qin, Y. Li, Y. He, C. Zhong, J. Pan, H. Dong, W. Xu, T. Li, W. Hu, J. L. Brédas, and O. M. Bakr, Spiro-OMeTAD single crystals: Remarkably enhanced charge-carrier transport via mesoscale ordering, *Sci. Adv.* **2**, e1501491 (2016).
- [24] G. Priebe and R. Könenkamp, Determination of transport parameters in fullerene films, *Appl. Phys. Lett.* **71**, 2160 (1997).
- [25] J. Cabanillas-Gonzalez, T. Virgili, A. Gambetta, G. Lanzani, T. D. Anthopoulos, and D. M. de Leeuw, Photoinduced transient stark spectroscopy in organic semiconductors: A method for charge mobility determination in the picosecond regime, *Phys. Rev. Lett.* **96**, 106601 (2006).
- [26] T. B. Singh, N. S. Sariciftci, H. Yang, L. Yang, B. Plochberger, and H. Sitter, Correlation of crystalline and structural properties of C60 thin films grown at various temperature with charge carrier mobility, *Appl. Phys. Lett.* **90**, 213512 (2007).
- [27] M. Monti, S. X. Tao, M. Staniforth, A. Crocker, E. Griffin, A. Wijesekara, R. A. Hatton, and J. Lloyd-Hughes, Efficient intraband hot carrier relaxation in the perovskite semiconductor $\text{Cs}_{1-x}\text{Rb}_x\text{SnI}_3$ mediated by strong electron-phonon coupling, *J. Phys. Chem. C* **122**, 20669 (2018).
- [28] M. Monti, K. D. G. I. Jayawardena, E. Butler-Caddle, R. M. I. Bandara, J. M. Woolley, M. Staniforth, S. R. P. Silva, and J. Lloyd-Hughes, Hot carriers in mixed Pb-Sn halide perovskite semiconductors cool slowly while retaining their electrical mobility, *Phys. Rev. B* **102**, 245204 (2020).
- [29] A. Ren, *et al.*, High-bandwidth perovskite photonic sources on silicon, *Nat. Photonics* **17**, 798 (2023).
- [30] M. Baranowski and P. Plochocka, Excitons in metal-halide perovskites, *Adv. Energy Mater.* **10**, 1903659 (2020).
- [31] G. Giorgi, J. I. Fujisawa, H. Segawa, and K. Yamashita, Small photocarrier effective masses featuring ambipolar transport in methylammonium lead iodide perovskite: A density functional analysis, *J. Phys. Chem. Lett.* **4**, 4213 (2013).
- [32] B. Krogmeier, F. Staub, D. Grabowski, U. Rau, and T. Kirchartz, Quantitative analysis of the transient photoluminescence of $\text{CH}_3\text{NH}_3\text{PbI}_3/\text{PC}_{61}\text{BM}$ heterojunctions by numerical simulations, *Sustain. Energy Fuels* **2**, 1027 (2018).
- [33] N. E. Courtier, J. M. Cave, A. B. Walker, G. Richardson, and J. M. Foster, Ionmonger: A free and fast planar perovskite solar cell simulator with coupled ion vacancy and charge carrier dynamics, *J. Comput. Electron.* **18**, 1435 (2019).

- [34] P. Calado, I. Gelmetti, B. Hilton, M. Azzouzi, J. Nelson, and P. R. Barnes, Driftfusion: An open source code for simulating ordered semiconductor devices with mixed ionic-electronic conducting materials in one dimension, *J. Comput. Electron.* **21**, 960 (2022).
- [35] S. Selberherr, *Analysis and Simulation of Semiconductor Devices* (Springer Vienna, Vienna, 1984).
- [36] F. Peña-Camargo, J. Thiesbrummel, H. Hempel, A. Musienko, V. M. Le Corre, J. Diekmann, J. Warby, T. Unold, F. Lang, D. Neher, and M. Stolterfoht, Revealing the doping density in perovskite solar cells and its impact on device performance, *Appl. Phys. Rev.* **9**, 021409 (2022).
- [37] T. W. Crothers, R. L. Milot, J. B. Patel, E. S. Parrott, J. Schlipf, P. Müller-Buschbaum, M. B. Johnston, and L. M. Herz, Photon reabsorption masks intrinsic bimolecular charge-carrier recombination in $\text{CH}_3\text{NH}_3\text{PbI}_3$ perovskite, *Nano Lett.* **17**, 5782 (2017).
- [38] J. D. Hutchinson, E. Ruggeri, J. M. Woolley, G. Delport, S. D. Stranks, R. L. Milot, J. D. Hutchinson, J. M. Woolley, R. L. Milot, E. Ruggeri, G. Delport, and S. D. Stranks, Resolving the ultrafast charge carrier dynamics of 2D and 3D domains within a mixed 2D/3D lead-tin perovskite, *Adv. Funct. Mater.* **33**, 2305736 (2023).
- [39] P. Schulz, L. L. Whittaker-Brooks, B. A. Macleod, D. C. Olson, Y. L. Loo, and A. Kahn, Electronic level alignment in inverted organometal perovskite solar cells, *Adv. Mater. Interfaces* **2**, 1400532 (2015).
- [40] J. P. McKelvey, *Solid State and Semiconductor Physics*, Harper's Physics Series (Harper & Row, New York, 1966).
- [41] D. W. Hahn and M. N. Özisik, *Heat Conduction: Third Edition* (John Wiley and Sons, Hoboken, New Jersey, 2012).
- [42] K. L. Luke and L.-J. Cheng, Analysis of the interaction of a laser pulse with a silicon wafer: Determination of bulk lifetime and surface recombination velocity, *J. Appl. Phys.* **61**, 2282 (1987).
- [43] A. B. Sproul, Dimensionless solution of the equation describing the effect of surface recombination on carrier decay in semiconductors, *J. Appl. Phys.* **76**, 2851 (1994).
- [44] M. G. Burdanova, A. P. Tsapenko, D. A. Satco, R. Kashtiban, C. D. W. Mosley, M. Monti, M. Staniforth, J. Sloan, Y. G. Gladush, A. G. Nasibulin, and J. Lloyd-Hughes, Giant negative terahertz photoconductivity in controllably doped carbon nanotube networks, *ACS Photonics* **6**, 1058 (2019).
- [45] J. Warby, F. Zu, S. Zeiske, E. Gutierrez-Partida, L. Frohloff, S. Kahmann, K. Frohna, E. Mosconi, E. Radicchi, F. Lang, S. Shah, F. Peña-Camargo, H. Hempel, T. Unold, N. Koch, A. Armin, F. De Angelis, S. D. Stranks, D. Neher, and M. Stolterfoht, Understanding performance limiting interfacial recombination in pin perovskite solar cells, *Adv. Energy Mater.* **12**, 2103567 (2022).
- [46] Y. Shao, Y. Yuan, and J. Huang, Correlation of energy disorder and open-circuit voltage in hybrid perovskite solar cells, *Nat. Energy* **1**, 1 (2016).
- [47] J. Liu, *et al.*, Efficient and stable perovskite-silicon tandem solar cells through contact displacement by MgF_2 , *Science* **377**, 302 (2022).
- [48] M. B. Johnston and L. M. Herz, Hybrid perovskites for photovoltaics: Charge-carrier recombination, diffusion, and radiative efficiencies, *Acc. Chem. Res.* **49**, 146 (2016).
- [49] D. Meggiolaro, E. Mosconi, and F. De Angelis, Mechanism of reversible trap passivation by molecular oxygen in lead-halide perovskites, *ACS Energy Lett.* **2**, 2794 (2017).
- [50] R. Brenes, C. Eames, V. Bulović, M. S. Islam, and S. D. Stranks, The impact of atmosphere on the local luminescence properties of metal halide perovskite grains, *Adv. Mater.* **30**, 1706208 (2018).
- [51] W. A. Quitsch, D. W. Dequillettes, O. Pfungsten, A. Schmitz, S. Ognjanovic, S. Jariwala, S. Koch, M. Winterer, D. S. Ginger, and G. Bacher, The role of excitation energy in photobrightening and photodegradation of halide perovskite thin films, *J. Phys. Chem. Lett.* **9**, 2062 (2018).
- [52] S. G. Motti, D. Meggiolaro, A. J. Barker, E. Mosconi, C. A. R. Perini, J. M. Ball, M. Gandini, M. Kim, F. De Angelis, and A. Petrozza, Controlling competing photochemical reactions stabilizes perovskite solar cells, *Nat. Photonics* **13**, 532 (2019).
- [53] M. Karakus, S. A. Jensen, F. D'Angelo, D. Turchinovich, M. Bonn, and E. Cánovas, Phonon-electron scattering limits free charge mobility in methylammonium lead iodide perovskites, *J. Phys. Chem. Lett.* **6**, 4991 (2015).
- [54] P. Farrell, N. Rotundo, D. H. Doan, M. Kantner, J. Fuhrmann, and T. K. S. E. D.-D. Models, in *Handbook of Optoelectronic Device Modeling and Simulation* (CRC Press, Boca Raton, 2017).
- [55] G. A. Evans, J. M. Blackledge, and P. D. Yardley, *Numerical Methods for Partial Differential Equations*, Springer Undergraduate Mathematics Series (Springer London, London, 2000).
- [56] D. Vasileska, S. M. Goodnick, and G. Klimeck, *Computational Electronics: Semiclassical and Quantum Device Modeling and Simulation* (CRC Press, Boca Raton, 2017).